Nanoscale Advances

ROYAL SOCIETY OF CHEMISTRY

PAPER

View Article Online
View Journal | View Issue

Cite this: *Nanoscale Adv.*, 2023, **5**, 3018

Dual imaging agent for magnetic particle imaging and computed tomography†

Sitong Liu,[a] Anahita Heshmat,[b] Jennifer Andrew,[c] Izabella Barreto[b] and Carlos M. Rinaldi-Ramos *[ad]

Magnetic particle imaging (MPI) is a novel biomedical imaging modality that allows non-invasive, tomographic, and quantitative tracking of the distribution of superparamagnetic iron oxide nanoparticle (SPION) tracers. While MPI possesses high sensitivity, detecting nanograms of iron, it does not provide anatomical information. Computed tomography (CT) is a widely used biomedical imaging modality that yields anatomical information at high resolution. A multimodal imaging agent combining the benefits of MPI and CT imaging would be of interest. Here we combine MPI-tailored SPIONs with CT-contrast hafnium oxide (hafnia) nanoparticles using flash nanoprecipitation to obtain dual-imaging MPI/CT agents. Co-encapsulation of iron oxide and hafnia in the composite nanoparticles was confirmed *via* transmission electron microscopy and elemental mapping. Equilibrium and dynamic magnetic characterization show a reduction in effective magnetic diameter and changes in dynamic magnetic susceptibility spectra at high oscillating field frequencies, suggesting magnetic interactions within the composite dual imaging tracers. The MPI performance of the dual imaging agent was evaluated and compared to the commercial tracer ferucarbotran. The dual-imaging agent has MPI sensitivity that is ~3× better than this commercial tracer. However, worsening of MPI resolution was observed in the composite tracer when compared to individually coated SPIONs. This worsening resolution could result from magnetic dipolar interactions within the composite dual imaging tracer. The CT performance of the dual imaging agent was evaluated in a pre-clinical animal scanner and a clinical scanner, revealing better contrast compared to a commercial iodine-based contrast agent. We demonstrate that the dual imaging agent can be differentiated from the commercial iodine contrast agent using dual energy CT (DECT) imaging. Furthermore, the dual imaging agent displayed energy-dependent CT contrast arising from the combination of SPION and hafnia, making it potentially suitable for virtual monochromatic imaging of the contrast agent distribution using DECT.

Received 16th February 2023
Accepted 30th April 2023

DOI: 10.1039/d3na00105a

rsc.li/nanoscale-advances

1. Introduction

Magnetic particle imaging (MPI) has attracted tremendous interest since its introduction in 2005.[1] In MPI, the non-linear magnetization response of superparamagnetic SPIONs (SPIONs) in an oscillating excitation field is used to generate a signal and construct an image. As a result, MPI has negligible signal from tissue, bones, or air gaps and has no tissue attenuation, resulting in distinct advantages over other imaging modalities.[2] The linear quantitative nature of MPI and its high sensitivity, detecting nanograms of iron per voxel,[3] has motivated use of MPI in diverse applications, such as cell tracking,[2] gut bleed detection,[4] drug delivery,[5] and imaging-guided hyperthermia.[6] However, because natural tissues do not generate MPI signal, MPI images lack anatomical reference information and require co-registration with other imaging modalities, such as computed tomography (CT).[7] However, motion artifacts can complicate precise multimodal image registration during sequential imaging. More recently, an MPI-CT hybrid scanner was reported, resulting in simultaneous MPI and CT measurements.[8] However, the CT contrast of common MPI tracers consisting of iron oxide is low because Fe is not an ideal CT contrast element. As such, a dual-mode imaging agent capable of sensitive MPI detection and strong CT contrast would be desirable.

CT relies on the transmission and attenuation of X-ray radiation to create images of internal structures and is widely used in clinical imaging.[9] Differences in mass attenuation between materials result in image contrast in CT. As a result,

[a]*Department of Chemical Engineering, University of Florida, Gainesville, FL 32611, USA. E-mail: carlos.rinaldi@ufl.edu*

[b]*Department of Radiology, University of Florida, Gainesville, FL 32610-0374, USA*

[c]*Department of Material Science and Engineering, University of Florida, Gainesville, FL 32603, USA*

[d]*J. Crayton Pruitt Family Department of Biomedical Engineering, University of Florida, Gainesville, FL 32611-6131, USA*

† Electronic supplementary information (ESI) available. See DOI: https://doi.org/10.1039/d3na00105a

structures with higher atomic numbers and density, such as bone, appear brighter compared to lighter materials, such as soft tissues. To facilitate observation of areas of interest that are less dense, contrast agents are normally introduced to patients. Among CT contrast agents, nanoparticles composed of gold, hafnium, and other materials with high electron density are of interest. Additionally, CT has an excellent spatial resolution in the hundreds-of-μm range, which is better than the current typical mm-scale resolution in MPI.[10–12]

Ferucarbotran is the most widely used commercially available tracer for MPI. However, it was not optimized for MPI and only 3% of its total mass contributes to its MPI signal.[1] We have previously reported the synthesis of an MPI-tailored SPION tracer that possesses ~3× MPI sensitivity compared to ferucarbotran.[13] Currently, iodine-based contrast agents are widely used in clinical CT. However, they are not optimal CT contrast agents according to simulations[14] and experiments.[15] Gold nanoparticles are also being investigated for CT due to superior contrast compared to iodine[16] and are commercially available for research use. However, the cost of gold is high compared to that of other dense metals.[17,18] The high electron density and chemical stability of hafnium oxide (HfO_2, hafnia) make its nanoparticle form a good candidate as a contrast agent for CT,[15] where it could be a more sensitive alternative to clinical iodine-based contrast agents and a more affordable alternative to gold nanoparticle contrast agents under development. Here we report the formulation of dual imaging agents consisting of these MPI-tailored iron oxide and CT-contrast enhancing hafnia nanoparticles.

Flash nanoprecipitation (FNP) is a process to produce nanoclusters. In this process, high supersaturation and kinetically controlled aggregation are achieved by rapid mixing. The result of the process is nanoclusters composed of hydrophobic compounds capped by block copolymers. Because the size and composition of the product is controlled by the raw material compositions of the impinging streams and the processing time, FNP is easily scalable to produce large quantities once ideal formulation conditions are identified using small screening volumes. FNP also has the capability of encapsulating more than one species of hydrophobic compound or nanoparticle per cluster. In the past, FNP has been used to assemble multimodal imaging nanocarriers consisting of magnetic nanoparticles for magnetic resonance imaging and molecular dyes for long-wavelength fluorescence imaging.[19] However, the formulation of composite nanoparticles consisting of more than one type of inorganic nanoparticle using FNP has not been reported.

Here we report the formulation of a new dual imaging agent composed of MPI-tailored SPIONs and CT-contrast hafnia nanoparticles using FNP. The SPIONs and the hafnia nanoparticles were both synthesized through thermal decomposition. The dual imaging agent was fabricated through FNP using poly (D,L-lactide) (PLA) as homopolymer co-core excipient and polylactic acid-*b*-polyethylene glycol (PLA-*b*-PEG) as the block copolymer outer layer. The physical and hydrodynamic properties of the nanoparticles and the dual imaging agents were evaluated. The MPI performance of the dual imaging agents was evaluated using a MOMENTUM™ MPI scanner while the CT performance of the dual imaging agents was assessed using a pre-clinical IVIS® SpectrumCT *In Vivo* Imaging System and using a clinical Aquilion ONE GENESIS scanner. The MPI and CT performance of the dual imaging agent nanoparticles were compared to those of the commercial imaging agents ferucarbotan for MPI and Omnipaque (contains iohexol as the active ingredient, manufactured by GE Health) for CT.

2. Methods

2.1. Particle synthesis

2.1.1. Materials. Iron(III) acetylacetonate (>98% pure) was purchased from TCI America (Portland, OR). Oleic acid (90% technical grade), docosane (90% pure), 1-octadecene (90% technical grade), triethylene glycol dimethacrylate (TEGDMA), 2,2′-azobis(2-methylpropionitrile), and potassium nitrate (>99%, ACS reagent) were purchased from Sigma-Aldrich (St. Louis, MO). Toluene (>99.5%, ACS reagent), ethanol (200 proof), acetone (certified ACS), hydrochloric acid (37% w/v), nitric acid (Certified ACS Plus), hafnium(IV) tetrachloride (99.9%), trifluoroacetic acid (reagent grade), tetrahydrofuran (THF, 99.8%, HPLC grade, unstabilized), MilliporeSigma™ Amicon™ Ultra Centrifugal Filter Units (100 kDa), and potassium hydroxide (85%, ACS reagent) were purchased from Thermo Fisher Scientific (Waltham, MA). Magnetic columns were purchased from Miltenyi Biotec (Germany). Ferucarbotran was purchased from Meito Sangyo Co., Ltd (Japan). Copper TEM grids (carbon film only, 200 mesh) was purchased from TED PELLA, INC (Redding, CA). Polylactic acid-*b*-polyethylene glycol (PLA-*b*-PEG, 6 kDa PLA, 4.9 kDa PEG) was purchased from Evonik Industries (Essen, Germany). Poly(D,L-lactide) (PLA, 10.3 kDa) was purchased from Polymer Source (Quebec, Canada). Omnipaque Contrast Solution (240 mg ml^{-1}), manufactured by GE Healthcare (Boston, MA) was purchased from Patterson Veterinary Supply (Devens, MA).

2.1.2. Synthesis of iron oleate. A stoichiometrically defined iron oleate was prepared according to published work with modification.[20] Iron(III) acetylacetonate (22.38 g, 63.36 mmol) and oleic acid (89.48 g, 316.80 mmol) were added to a 500 ml three-neck reactor. The flask was equipped with a Caframo compact overhead stirrer in the middle neck, a septum with a thermocouple, and a stainless steel (SS) needle through the left neck. 100 sccm of argon was continuously running through the SS needle during the synthesis, controlled using mass flow controller from Alicat Scientific. A condenser connecting to a chiller was attached in the right neck. The reaction vessel was equipped with a molten metal bath as a heating source controlled using a temperature controller. The molten metal was heated to 110 °C before submerging the reaction vessel into the molten metal bath. The reaction mixture was then heated to 310 °C under stirring at 350 rpm. After 30 min since the reaction mixture reached 300 °C, the reaction was stopped to obtain a dark brown waxy liquid. The obtained iron oleate was purged using argon before using for nanoparticle synthesis.

2.1.3. Synthesis of SPIONs. SPIONs were synthesized as described in a previous publication.[13] Docosane (10.1 g, 32.23

mmol) and oleic acid (6.23 g, 22.06 mmol) were added to a 100 ml three-neck reactor. Separately, iron oleate was mixed with 1-octadecene (27.12 g, 107.40 mmol) to prepare a precursor with 0.22 M Fe. The flask was equipped with an overhead stirrer in the middle neck and a septum with an SS needle through the left neck. A molten metal bath was used as the heating source combined with a temperature controller. The molten metal was heated to 110 °C before submerging the reaction vessel into the molten metal bath. The mixture was heated to 350 °C in 30 min before the controlled addition of iron oleate precursor (1.98) using a syringe pump. Nitrogen (100 sccm) was supplied continuously through the SS needle, controlled using a mass flow controller until the reaction mixture reached 360 °C. Then, 140 sccm of 1% oxygen in argon mixture was introduced into the reactor headspace through the SS needle, controlled using a mass flow controller. Uniform mixing at 350 rpm was maintained throughout the reaction. The precursor drip was stopped after 4 hours, and the reactor was removed from the molten metal bath. Toluene and ethanol in a 1 : 1.5 volume ratio was used to precipitate nanoparticles from the crude synthesis product. Purified oleic acid-coated particles were suspended in toluene for physical characterization and suspended in THF for iron quantification and flash nanoprecipitation. Both suspensions were stored at 4 °C before use.

2.1.4. Synthesis of trifluoroacetate hafnium(IV). Trifluoroacetate hafnium(IV) was synthesized following the protocol previously described by Liu *et al.* with modification.[21] Hafnium(IV) chloride (9.6 g) was charged in a 100 ml 3-neck reactor. The flask was equipped with an overhead stirrer in the middle neck, a septum with a thermocouple, and an SS needle through the left neck. Argon (50 sccm) was supplied continuously through the SS needle during synthesis, using a mass flow controller. Trifluoroacetic acid (50 ml) was added to the reactor over 1 min while stirring at 100 rpm. The stirring rate was changed to 300 rpm after the addition of trifluoroacetic acid. A condenser connecting to a chiller was attached in the right neck and the top of the condenser was connected to a standard backflow prevention setup with a water-filled beaker. The reaction mixture was heated to a temperature of 40 °C at a rate of 5 °C min^{-1} using a heating mantle followed by soaking for 5 hours. At the end of the reaction, the reaction mixture was transferred to a 100 ml 1-neck round bottom flask for rotary evaporation at Labvac mode to remove excess trifluoroacetic acid over a period of 3 h. The resulting white solid trifluoroacetate hafnium(IV) was stored in a vacuum desiccator until used for nanoparticle synthesis.

2.1.5. Synthesis of hafnia. Hafnia nanoparticles were synthesized as previously described with modifications.[21] Trifluoroacetate hafnium(IV) (2.54 g) and oleylamine (53 ml) were added to a 100 ml three-neck reactor. The flask was equipped with an overhead stirrer in the middle neck and a septum with an SS needle through the left neck. A molten metal bath and temperature controller were used as the heating source. The molten metal was heated to 110 °C before pushing the reaction vessel into the molten metal bath. The reaction mixture was soaked for 30 min at 110 °C before being heated to 330 °C for 60 min. Argon (100 sccm) was supplied continuously through the SS needle, controlled using a mass flow controller. Uniform mixing at 350 rpm was maintained throughout the reaction. The reaction was stopped 1 hour after reaching the target temperature and the reactor was removed from the molten metal bath. Acetone (1×) was used to precipitate the particles at a ratio of 3 : 1, followed by addition of toluene and ethanol (3×) in a 1 : 2 volume ratio. Purified oleylamine coated particles were suspended in toluene and stored at 4 °C before use. To measure the hafnia concentration in toluene, 100 μl of particle solution was added to a pre-weighed empty glass vial before drying overnight, followed by weighing to calculate the mass of dry particles. Thermogravimetric analysis (TGA) was then performed on 5–10 mg of dried particles to determine the organic and inorganic mass fractions. The calculated inorganic mass fraction was used to calculate the inorganic mass in the original particle solution. Aliquots containing 4.5 mg of hafnia nanoparticles in toluene were added to a 4 ml dry, empty glass vials, subjected to vacuum overnight to remove toluene, and then placed in a vacuum desiccator for storage before being used in flash nanoprecipitation (FNP).

2.2. Composite particle fabrication

Three solutions, one containing 10 mg ml^{-1} PLA-*b*-PEG, one containing 0.75 mg ml^{-1} hafnia nanoparticles and 0.75 mg ml^{-1} SPIONs, and one containing 5 mg ml^{-1} PLA in THF were prepared. Two 50 ml airtight syringes (Model 1050 TLL, PTFE Luer Lock, Hamilton Company, Reno, VA) were each loaded with 10 ml of the nanoparticle/PLA in THF mixture and with 10 ml of the PLA-*b*-PEG in THF solution. Two 50 ml airtight syringes were loaded with 10 ml DI water. These four syringes were connected to a multi-inlet-vortex-mixer (MIVM) with two water syringes opposite to each other and were pushed through the MIVM at approximately 60 ml min^{-1} using two PHD ULTRA™ syringe pumps (Harvard Apparatus, Holliston, MA). The resulting product was recovered in a 300 ml beaker containing 180 ml of deionized water. For the removal of THF and composite particles with no SPIONs, magnetic filtration was performed using magnetic columns (Miltenyi Biotec, Germany). For the concentration of the dual imaging agents after magnetic filtration, MilliporeSigma™ Amicon™ Ultra Centrifugal Filter Units (100 kDa) were used with centrifugation. The final iron oxide concentration in the dual imaging agent suspension was quantified using an iron-quantification assay. The final hafnia concentration in the dual imaging agent suspension was quantified by TGA as described above. The hafnia mass was estimated by subtracting the iron oxide mass from the inorganic mass determined by TGA.

2.3. SPION nanoparticle coating with PEG-silane

SPIONs were coated with PEG-silane using ligand exchange, replacing the oleic acid on the surface of the SPIONs with PEG-silane, following procedures similar to Liu *et al.*[13] Briefly, 0.7 g of PEG-silane was dissolved in 4 ml of dry toluene. Once the PEG-silane was dissolved, 2 ml of SPIONs at 2.5 mg Fe_3O_4 per ml and 28 μl of APS were added and mixed. The solution was capped and allowed to react overnight, approximately 16 hours,

in a heating block set at 100 °C. The next day, the PEG-silane coated SPIONs were precipitated out of solution using cold diethyl ether. The sample was centrifuged and supernatant discarded. The SPIONs were resuspended in acetone and precipitated again with cold diethyl ether twice. The precipitate was then dried in a vacuum oven at room temperature overnight. The following day, PEG-silane coated SPIONs were resuspended in water and dialyzed to remove excess PEG-silane. For further purification, particles were purified using magnetic columns. The resulting nanoparticles were backfilled with additional PEG-COOH using EDC-NHS chemistry. The number of remaining primary amines on the particles was quantified using the CBQCA protein quantification kit, following the manufacturer's protocol. Once the number of amines were determined, a ratio of 1 : 2 amine to carboxylic acid was used. The mPEG-COOH was suspended in water and pH adjusted to 5.0. EDC was added at a 1 : 2 carboxylic acid : EDC ratio and allowed to react for 15 minutes. Then, sulfo-NHS was added at a 1 : 1 ratio of EDC to sulfo-NHS. The pH of the solution was slowly adjusted to 7.0 and reacted for 15 minutes. Last, the nanoparticle solution was added and the pH adjusted to 9.0. The mixture reacted overnight and was purified using a magnetic column. Finally, the nanoparticles were sterilized using a 0.22 μm PES syringe filter.

2.4. Physical, hydrodynamic, and fluorescence characterization

2.4.1. Transmission electron microscopy. Images of iron oxide, hafnia, and composite nanoparticles sampled on 200-mesh copper grids with carbon film were acquired using a FEI Talos™ F200i S/TEM. Physical diameters (D_p) were obtained by analyzing the images using Fiji. Reported size distribution statistics and histograms are based on at least 2000 particles for SPIONs and hafnia nanoparticles.[22]

The number median diameter (D_{pg}) and geometric standard deviation ($\ln \sigma_g$) of the particle size distribution were obtained by fitting the size distribution histograms to the lognormal distribution ($n_N(D_p)$) using[23]

$$n_N(D_p) = \frac{1}{\sqrt{2\pi} D_p \ln \sigma_g} \exp\left(- \frac{\ln^2 D_p / D_{pgv}}{2 \ln^2 \sigma_g} \right) \quad (1)$$

D_{pg} was converted to a volume median diameter (D_{pgv}) using[23]

$$D_{pgv} = \exp[\ln D_{pg} + 3 \ln^2 \sigma_g] \quad (2)$$

The arithmetic volume weighted mean diameter (D_{pv}) and standard deviation (σ) were calculated using[20]

$$D_{pv} = \exp\left(\ln D_{pgv} + \frac{\ln^2 \sigma_g}{2} \right) \quad (3)$$

$$\sigma = D_{pv} \sqrt{\exp(\ln^2 \sigma_g - 1)} \quad (4)$$

The composition of the dual imaging agents was analyzed using energy-dispersive X-ray spectroscopy (EDS) using a FEI Talos™ F200i S/TEM equipped with a Bruker XFlash™ 6T/30 windowless silicon drift detector EDS system and a Fischione Instruments Model 3000™ high angle annular dark field (HAADF) scanning transmission electron microscopy (STEM) detector, which allowed us to obtain high-resolution elemental maps of the dual imaging agents. In this step, the nanoparticles were embedded in a TEGDMA matrix as described below. A staff member from the Research Service Center at the University of Florida performed the analysis.

To prepare samples embedded in TEGDMA, a concentrated nanoparticle suspension in water was mixed with TEGDMA monomer at a particle concentration of 0.1 wt%. The initiator 2,2′-azobis(2-methylpropionitrile) was added at a concentration of 0.05 wt%, and crosslinking was performed by heating the mixture at 70 °C for 6 h.

2.4.2. Dynamic light scattering and zeta potential. A Brookhaven Instruments ZetaPALS dynamic light scattering and zeta potential measurement instrument, operating at a scattering angle of 90° at room temperature, was used to determine the hydrodynamic size and zeta potential of the SPIONs. For hydrodynamic diameter measurements, particles at 1 mg ml^{-1} were suspended in deionized water, resulting a final particle concentration of 0.01 mg ml^{-1}. The zeta potential of the particles was measured in a 1 mM KNO_3 solution at pH 7, adjusted with nitric acid and potassium hydroxide.

2.4.3. Magnetic characterization. Magnetic characterization was performed with the particles suspended in water at 300 K to obtain magnetization data for the purpose of magneto-granulometry to obtain magnetic diameters. For comparison purposes, measurements were also made for SPIONs coated with PEG-silane as described in previous publication[13] to indicate single-particle behavior.

Magnetic diameters (D_m) and the geometric standard deviation (σ_g) of the SPIONs at various time points were obtained by fitting the magnetization curves to the Langevin function $L(\alpha)$ for superparamagnetism, weighted using a lognormal size distribution ($n_v(D_m)$) as suggested by Chantrell *et al.*[24] In the equations, α is the Langevin parameter, M_S is the saturation magnetization of the sample, $L(\alpha)$ is the Langevin function, μ_0 is the permeability of free space, M_d is the domain magnetization (446 000 A m^{-1}),[25] and k_B is Boltzmann's constant.

$$M(\alpha) = M_S \int_0^\infty n_v(D_m) L(\alpha) \mathrm{d}D_m \quad (5)$$

$$n_v(D_m) = \frac{1}{\sqrt{2\pi} D_m \ln \sigma_g} \exp\left[- \frac{\ln^2 \left(\frac{D_m}{D_{pgv}} \right)}{2 \ln^2 \sigma_g} \right] \quad (6)$$

$$L(\alpha) = \coth\alpha - \frac{1}{\alpha} \quad (7)$$

$$\alpha = \frac{\pi \mu_0 M_d D_m{}^3 H}{6 k_B T} \quad (8)$$

Magnetization curves of SPIONs and the dual imaging agents were obtained using a Magnetic Property Measurement System 3 (MPMS 3, Quantum Design) superconducting quantum interference device (SQUID) magnetometer at room temperature in a PTFE sample holder with 100 μl of SPIONs or the dual imaging agents suspended in toluene. The volume median magnetic diameter was converted to volume mean magnetic diameter and standard deviation using eqn (3) and (4).

The dynamic magnetic susceptibility of all tracers in liquids (200 μl of total volume) of different viscosities were measured using a DynoMag AC susceptometer (Rise Research Institutes, Sweden) in a small amplitude oscillating magnetic field at a constant temperature and as a function of the frequency of the oscillating magnetic field. Samples used as comparison were SPIONs coated with oleic acid from synthesis after purification and the dual imaging agents.

2.4.4. Iron quantification. A suspension containing 10 μl of SPIONs suspended in toluene was digested using 1 ml of 70% nitric acid overnight at a temperature of 101 °C. Then, 10 μl of the digested sample was dried before diluting with 46 μl of DI water. Afterward, 30 μl of 8.06 M hydroxylamine hydrochloride was added to the water suspension and allowed to react for 1 h before the addition of 75 μl of 13 mM 1,10-phenanthroline monohydrate to form an iron chelate. This was followed by addition of 49 μl of 1.22 M sodium acetate to neutralize unreacted hydroxylamine hydrochloride. Then, 100 μl of the prepared sample was taken in triplicate for absorbance measured at 508 nm using a SpectraMax M5 microplate reader. A calibration curve was obtained using a dilution series prepared from an iron ICP standard stock solution (Fluka). Iron concentration from each sample was acquired by relating absorbance to the calibration curve.

2.5. MPI performance

To image the sample in the MPI scanner, a sample holder designed in a previous publication was used.[13] For relax scan measurements, 10 μl of the dual imaging agents and ferucarbotran were placed in separate 0.2 ml microcentrifuge tubes, and samples were centered in the FOV. Then, the *x*-space point spread function (PSF) was measured using the RELAX™ module in the MOMENTUM™ scanner.[26] The PSF was normalized by the iron mass to facilitate comparison across particles. The signal intensity was calculated by normalizing the system-reported amplitude using iron mass, and the full width at half maximum (FWHM) is the system-reported value.

For a visual comparison of the dual imaging agents and ferucarbotran, 2D images were acquired with the MOMENTUM™ scanner (Magnetic Insight, CA, USA) using high-sensitivity (3 T m^{-1}) multichannel scan mode (*x*- and *z*-channel scans). All samples consisted of 3 μl of solution (containing 5 μg_{Fe}) in a capillary tube (1/32″ ID) placed parallel to the *y*-axis in the field of view (FOV).

2.6. CT performance

2.6.1. Dilution series preparation. Dilution series according to the molar concentration of iodine or hafnium, from 1 mM to 25 mM, was prepared. The iodine concentration provided by the manufacturer and the hafnium concentration from TGA data was used.

2.6.2. Image acquisition and analysis in the IVIS® spectrum *in vivo* imaging system. For the IVIS® SpectrumCT *In Vivo* Imaging System, 200 μl of each of the contrast agents at various concentration were placed in separate 0.2 ml microcentrifuge tubes for imaging. Measurements were made in CT only mode for a standard one mouse field of view at a voltage of 50 kV and current of 1 mA, at medium resolution.

Images obtained from the SpectrumCT were stored as DICOM files. Each DICOM file contained data from a set of three vials in the dilution series. These DICOM files were analyzed using 3D Slicer to quantify the CT attenuation of each dilution. First, images were processed to allow for visualization of the vial contents. A threshold was applied to each image, followed by a volume rendering of the samples. After visualization was complete, segmentation was performed on each image to identify the contents of each individual vial and mark it for further analysis. Once each segmentation was obtained, segmentation statistics were calculated through the software. For each vial (segmentation), the mean intensity of the signal was reported from the segmentation statistics. These mean intensities were averaged across each dilution to obtain the average intensity for the dilution. The images acquired using the IVIS® Spectrum *In Vivo* Imaging System have air as the background. Therefore, manual water subtraction from the total signal was performed using the water signal acquired using the same equipment settings.

2.6.3. Image acquisition and analysis in a clinical CT system. To acquire the images, the contrast agents and water were filled into 200 μl microcentrifuge tubes at a range of hafnium oxide or iodine concentrations (1 mM to 50 mM). Here hafnium oxide concentration was used because this compound is the active ingredient in the dual imaging agent for CT. Similarly, iodine concentration was used for the calculations. Note that the active ingredient in Omnipaque is iohexol and each mole of iohexol has three moles of iodine. As a result, iodine concentration is 3× iohexol concentration. The sample holder with the tubes was placed in a plastic jar filled with water to mimic an in-human environment. Dual-Energy CT (DECT) and Subtraction CT (SCT) images were acquired with a 320-detector CT scanner (Aquilion ONE Genesis Edition, Canon Medical Systems USA, Inc., Tustin, CA). The jar containing the water and samples was scanned with the clinical head DECT protocol and with an SCT protocol for head CT angiography (CTA) indicated in Table 1 as described in a previous publication.[27] An SCT protocol was used to remove the background and the water signal. In SCT, a pre-and a post-contrast image are taken, and digital subtraction is performed, resulting in the removal of the background. As a result, the readings were already water signal subtracted. Since the SCT protocol requires both pre- and post-contrast images, the jar with water was first scanned for the initial non-contrast image and the tubes containing contrast agents were inserted for the scans of the post-contrast images. For DECT images, DECT raw data software was used to reconstruct iodine maps and virtual non-contrast (VNC)

Table 1 Scan and reconstruction parameters for SCT and DECT

	SCT	DECT
Protocols	CTA head	Head
Tube voltage (kV_p)	120	135 & 80
$CTDI_{vol}$ (mGy)	53.0	54.6
Tube current (mA)	400	100 & 570
Rotation time (s)	0.5	0.5
Field of view (mm)	220.3	220.3
Bowtie filter size	S	S
Reconstruction kernel	FC64	FC64/13
Iterative reconstruction method	AIDR-3D (mild strength)	AIDR-3D (mild strength)
Slice thickness (mm)	1.0	1.0
Pitch	0.625	0.625
Field of view	200×200 mm^2	200×200 mm^2
Detector configuration	320×0.5 mm	320×0.5 mm

images from the virtual monochromatic images (VMI). The iodine map images show the Omnipaque contrast agent, while the VNC images subtracts the iodine-containing contrast agent and only display other materials in the VMI, which in this case displays water and the dual imaging agents.

The post-reconstructed DECT and SCT images were obtained using the DECT and SCT software tools on the scanner's clinical tab to create the VMI, IM, and VNC images for DECT and the subtracted image for SCT. Furthermore, these images were evaluated quantitatively with a MATLAB® (MathWorks, MA, USA) script to extract regions of interest (ROIs) for each contrast agent at various concentrations. The mean CT numbers, standard deviations, and contrast-to-noise (CNR) ratios were determined.

3. Results and discussion

3.1. Hafnia nanoparticle and SPION synthesis, composite particle fabrication, and characterization

The synthesized SPIONs and hafnium oxide nanoparticles were evaluated using transmission electron microscopy (TEM). As shown in Fig. 1, the SPIONs and hafnium oxide nanoparticles are both single-core with narrow size distributions. The histograms of the physical size distribution for both nanoparticles are shown in Fig. S1.† The volume-weighted mean physical diameter was 19.4 nm and the standard deviation was 1.56 nm for SPIONs, while the volume-weighted mean physical diameter was 5.4 nm and the standard deviation was 0.82 nm for the hafnia nanoparticles. The coefficients of variation of the SPIONs and the hafnia nanoparticles are 0.08 and 0.15, respectively.

The dual imaging agents were prepared through FNP using PLA-*b*-PEG as the block copolymer and PLA as homopolymer co-core excipient. Magnetic filtration was used to remove THF and concentrate the product. Then ultrafiltration was carried out to further concentrate the dual imaging agents. Structure and hydrodynamic properties were assessed using TEM and DLS. Visualization from TEM images of several different dual imaging agents suggests the particles consist of clusters that are well separated from each other, as shown in Fig. 1C. Here, the co-localization of SPIONs and hafnia nanoparticles in each composite nanoparticle was observed consistently in all the composite nanoparticles. Due to their large size difference and narrow size distributions, it was relatively easy to distinguish iron oxide and hafnia nanoparticles from TEM according to size and shape. The intensity-weighted mean diameter of 129 nm and standard deviation of 44 nm was obtained from DLS measurements (Fig. 1D). Three batches of the dual imaging agents were measured against DLS to show reproducibility in hydrodynamic diameter (Fig. S2†). The zeta potential was determined at the physiological pH of 7.2–7.4 and was $\zeta = 3.7$ mV. A short-term study was undertaken to assess stability of the dual imaging agents, at a concentration of 5 mg ml^{-1} (inorganic mass), in phosphate buffered saline (PBS), Dulbecco's modified eagle's medium (DMEM), and DMEM + 10% fetal bovine serum (FBS). The particle concentration was chosen based on prior studies evaluating hafnia nanoparticles for radiotherapy.[28] At such a high concentration, the accuracy of the DLS measurement may be affected. Therefore, we chose to observe precipitate formation with respect to time to evaluate stability against gravitational settling. The dual imaging agent suspensions in all media were clear (not cloudy) and unchanged over a period of 6 hours, but precipitate was observed after 24 hours. This suggests that the dual imaging agent is stable at a high concentration for at least 6 hours. We note that similarly formulated composite nanoparticles containing only iron oxide were found to be stable against aggregation in complex biological fluids like synovial fluid,[29] thus we attribute observation of precipitate to gravitational settling over a period of 24 hours, rather than to aggregation of the particles that are coated with a PEG brush.

To further confirm the successful co-encapsulation of both inorganic nanoparticles in the composite dual imaging agents, EDS spectrum and mapping were performed under STEM mode on a sample of dual imaging agents embedded in TEGDMA. Fig. 2 shows a bright-field TEM image, a high-angle annular dark-field scanning transmission electron microscopy (HADDF) image, and elemental mapping images of a dual imaging agent. This analysis confirms the co-encapsulation of iron oxide and hafnia nanoparticles, which can be distinguished based on their HADDF contrast and their elemental composition.

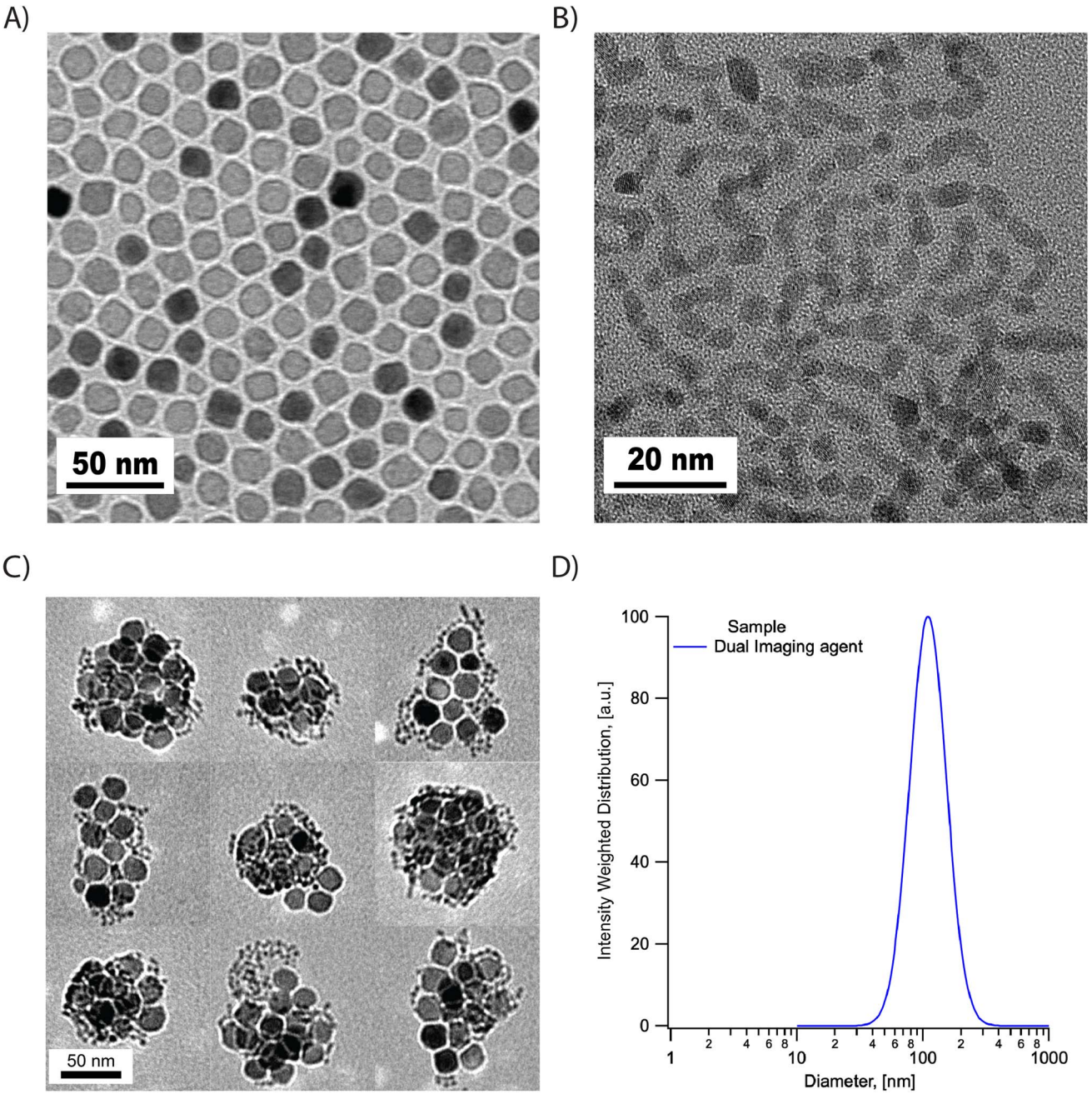

Fig. 1 Nanoparticles and nanoclusters evaluated *via* transmission electron microscopy (TEM) and dynamic light scattering (DLS). (A) TEM images of SPIONs. (B) TEM images of hafnium oxide nanoparticles. (C) Representative TEM images of dual imaging agents. (D) Representative DLS analysis of dual imaging agents.

The weight percentage of SPIONs and hafnium oxide nanoparticles in the composite nanoparticles were evaluated using iron quantification and TGA, as explained in the methods section. Representative TGA data is shown in Fig. S3.† Iron oxide concentration was obtained through the 1,10-phenanthroline assay. Combining both data, the iron oxide and hafnium oxide concentrations were determined to be 30.9 mg ml^{-1} and 12.3 mg ml^{-1}, respectively. We observe that with an equal mass ratio as raw material to start with, the final product inorganic mass consists of 72% of iron oxide and 28% of hafnia nanoparticles. This is likely due to the uneven distribution of hafnia and SPIONs in composite nanoparticles. Magnetic separation, a method that only keeps magnetic content, was used for purification and likely caused the removal of composite nanoparticles that only contained hafnia nanoparticles or very little iron oxide. Considering the sensitivity of MPI is much higher than that of CT, it is preferable to fabricate composite nanoparticles that possess a higher mass fraction of hafnium instead of iron. Future studies will evaluate the control of the hafnium to iron oxide mass ratio in these dual imaging agents.

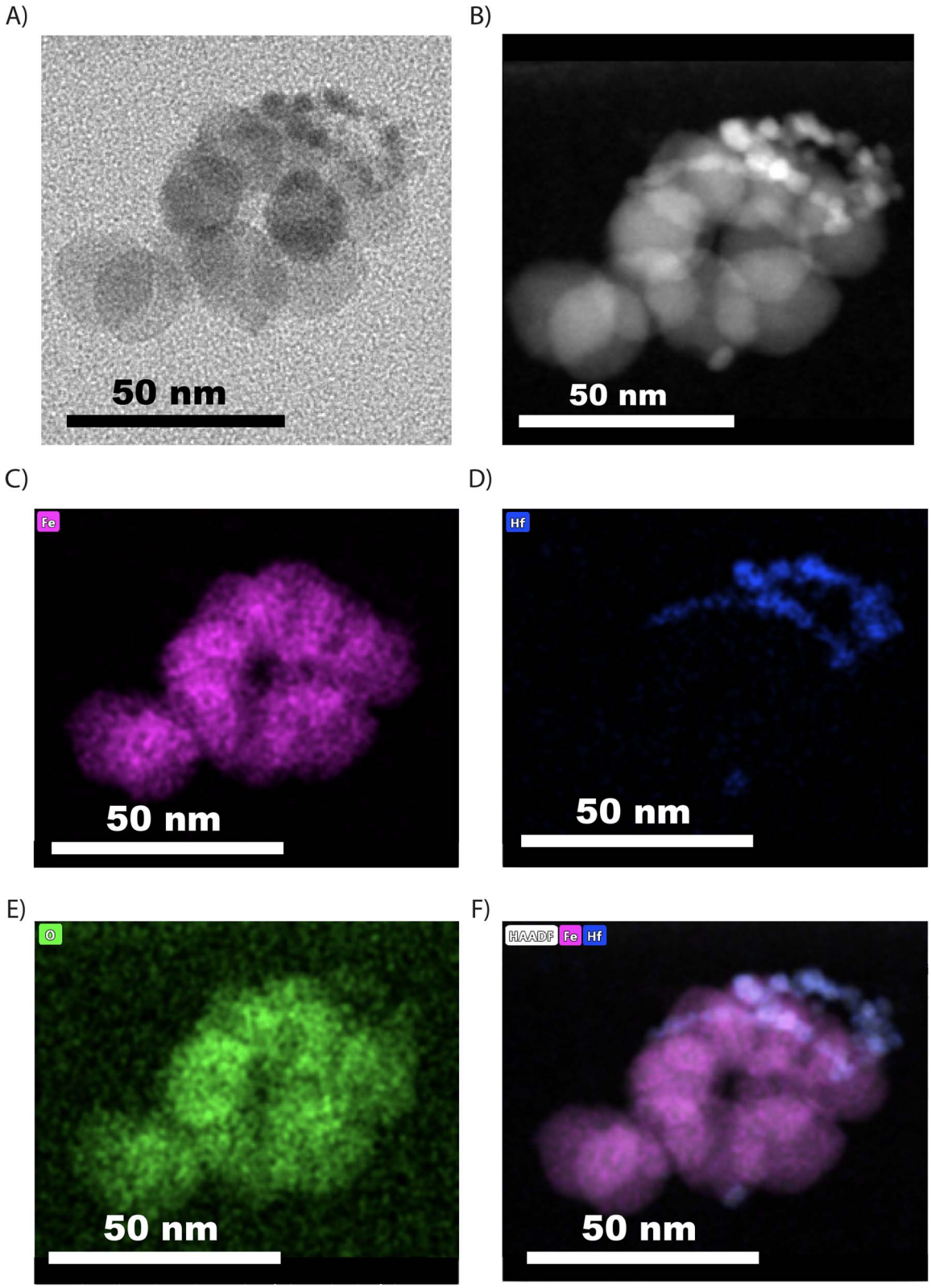

Fig. 2 Bright-field TEM image, HADDF STEM image, and elemental mapping images of dual imaging agents. (A) Bright-field TEM. (B) HADDF STEM image. (C) Elemental mapping showing iron content. (D) Elemental mapping showing hafnium content. (E) Elemental mapping showing oxygen content. (F) Superposition of iron, hafnium, and HADDF STEM images.

Magnetic characterization was carried out to evaluate the composite nanoparticles' magnetic properties. Magnetization *versus* magnetic field curves was obtained for the dual imaging agents and compared to those for the same SPIONs coated with PEG-silane. Here, we are interested in determining whether magnetic properties changed after encapsulation as a cluster in a polymeric nanoparticle. According to a previous study,[30] motion artifacts may affect magnetization measurements of large magnetic nanoparticles, possibly due to chain formation. This artifact can be significant when the nanoparticles are coated with oleic acid only and suspended in toluene. In contrast, magnetic nanoparticles coated with PEG-silane and suspended in water experience minimum motion artifacts. As such, PEG-silane-coated nanoparticles were used for comparison.

MH curves for both samples and the corresponding magnetic diameter distributions are presented in Fig. 3. The saturation magnetization was normalized using iron mass in the sample quantified by 1,10-phenontroline assay, as explained in the methods section. The saturation magnetization was 64.7 $Am^2\ kg^{-1}$ for the single-coated iron oxide and 57.07 $Am^2\ kg^{-1}$ for the dual imaging agents. This suggests a reduction of saturation magnetization after encapsulating the nanoparticles in the dual imaging agents. Fitting the data to the Langevin function weighted with a lognormal size distribution suggests that the singly coated SPIONs had an arithmetic volume-weighted mean magnetic diameter of 16.7 nm with standard deviation of 3.0 nm, whereas the composite dual imaging agents had an arithmetic volume-weighted mean magnetic diameter of 13.5 with standard deviation of 1.0 nm. This

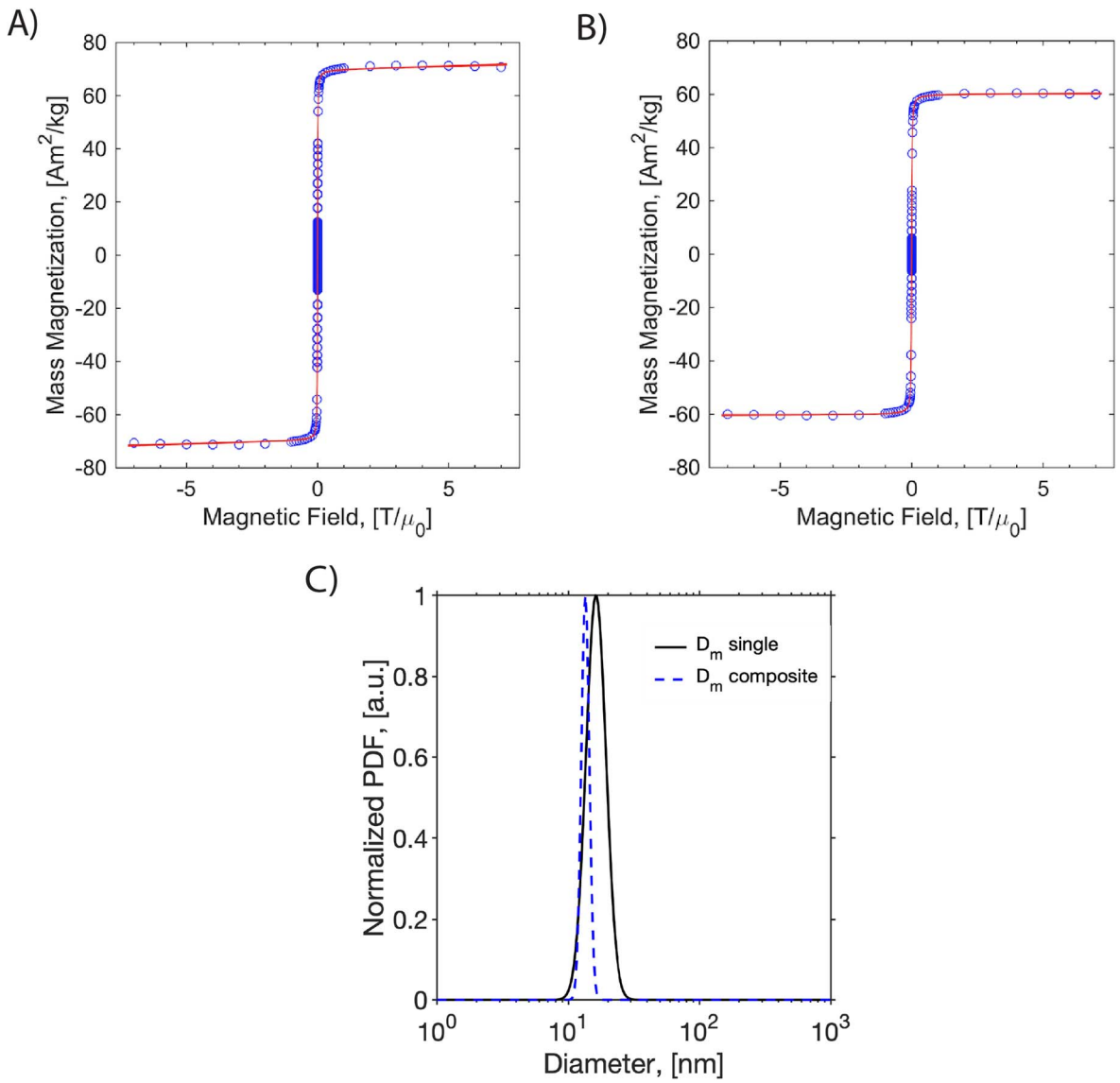

Fig. 3 Magnetization *versus* magnetic field curves obtained using a SQUID magnetometer. (A) SPIONs singly coated with PEG-silane. (B) Dual imaging agents. (C) Histogram of magnetic diameters for nanoparticles singly coated with PEG (single particles with a polymer corona) and dual imaging agents (composite nanoparticles).

suggests that the magnetic diameter of the SPIONs decreased by about 3 nm due to encapsulation in the composite dual imaging agents. The reduction of both saturation magnetization and the magnetic diameter suggests magnetic interactions between the nanoparticles inside the composite dual imaging agents.[31]

Dynamic magnetic susceptibility measurements were made for the dual imaging agent and oleic acid-coated particles to study their relaxation mechanism (Fig. S4†). Magnetic nanoparticles respond to time-varying magnetic fields by internal dipole rotation (*i.e.*, Néel relaxation) or physical particle rotation (*i.e.*, Brownian relaxation), with each mechanism being sensitive to the properties of the particles and the surrounding medium. It is essential to characterize the mechanism of SPION magnetic relaxation because this can impact their MPI performance.[11] We have previously determined that the PEG-coated SPIONs produced here undergo primarily Néel relaxation.[13] However, the closely packed SPIONs in the composite dual imaging agents could be subjected to internal particle–particle interactions, resulting in Brownian relaxation. As seen in Fig. S3,† the composite nanoparticles behave similarly to the oleic acid-coated particles and still undergo Néel relaxation. We note that no peak is observed in the out-of-phase susceptibility at a frequency of 1200 rad s^{-1}, as would be expected for a nanoparticle with a hydrodynamic diameter of ~130 nm undergoing Brownian relaxation in water. However, the shape of the complex susceptibility spectrum has changed in the high-frequency range. This suggests the composite nanoparticles may experience some particle–particle magnetic interactions, which is consistent with the observed reduction in magnetic diameter.[31]

3.2. Evaluation of MPI performance

We evaluated the MPI performance of the dual imaging agents and compared it to the commercial tracer ferucarbotran. MPI performance was characterized according to the PSF using the MPI RELAX™ module (Fig. 4). The RELAX™ module in the MOMENTUM™ measures the magnetization for a field sweep between −160 and 160 mT using a 16 mT, 45 kHz excitation field. The PSF is related to the derivative of the Langevin function and characterizes the performance of SPIONs in x-space MPI.[32] The PSF was used to determine the signal intensity (peak height) per iron mass, which measures expected particle sensitivity in MPI, and to obtain the full-width half-maximum (FWHM), which relates to the expected resolution in MPI. Representative PSF results for both tracers are shown in Fig. 3A. The MPI maximum signal intensity value for the dual imaging agents is 78 mg_{Fe}^{-1}, while the corresponding value is 28 mg_{Fe}^{-1} for ferucarbotran. In terms of resolution, the dual imaging agents have a FWHM of 17.2 mT, while the corresponding value was 11.4 mT for ferucarbotran. The spatial FWHM in units of mm was calculated assuming a field gradient of 5.7 T m^{-1}, resulting in expected spatial resolutions of 3.0 mm for dual imaging agents and 2.0 mm for ferucarbotran. The PSF data suggests that the dual imaging agents have better sensitivity than ferucarbotran, but a worse resolution. Interestingly, the resolution of the composite dual imaging agents was also worse compared to singly coated RL-1 nanoparticles from a previous publication,[13] where it was in the range of 11.4 to 13 mT. Compared to singly coated RL-1 nanoparticles, the worse resolution in the dual imaging agents could be attributed to magnetic dipolar interactions between the SPIONs in the composite nanoparticle core, as has been shown for iron oxide clusters formed by dropwise nanoprecipitation.[31] This is consistent with the observed reduction in saturation magnetization and magnetic diameter and the change in the high frequency range of the DMS spectrum. Fig. 3B also suggests a higher signal per unit mass for the dual imaging agents imaged in 2D high-sensitivity scan mode (3.055 T m^{-1} gradient strength, 15.5 mT RF excitation in the *x*-channel, and 20.5 mT RF excitation in the *z*-channel) compared to ferucarbotran.

3.3. Evaluation of CT contrast

We evaluated the performance of the dual imaging agents and compared them to the commercially available, clinically used iodinated contrast agent Omnipaque in two different scanner systems at various concentrations. The IVIS® SpectrumCT *In Vivo* Imaging System is typically used to acquire anatomical reference images, such as skeletal anatomy, for use in multimodal optical, fluorescence, and bioluminescence imaging. On the other hand, the Aquilion ONE GENESIS scanner system is a commercially available CT scanner commonly used in hospitals with human patients. Here, we evaluate the performance of the dual imaging agents for both research and clinical use.

As seen in Fig. 5, the grayscale images from both scanners suggest that the dual imaging agents have a stronger signal intensity than Omnipaque at equal Hf/I concentrations. The mean signal intensity *versus* concentration for both contrast agents in both scanners is shown in Fig. 5C and D. Both systems demonstrated a linear relationship between X-ray attenuation and concentration for both contrast agents. According to the fitting, the signal intensity of the dual imaging agents was 3.5× and 1.5× higher compared to Omnipaque in the IVIS® SpectrumCT *In Vivo* Imaging System and in the Aquilion ONE GENESIS scanner SCT protocol, respectively.

To understand the contribution of SPIONs to the X-ray attenuation, formulation of hafnia nanoparticle clusters (HNCs) using FNP containing only hafnia nanoparticles was conducted. Here, HNCs were used for comparison instead of oleylamine-coated hafnia nanoparticles because the latter can only be suspended in organic solvents, which we could not use in the clinical Aquilion ONE GENESIS scanner. For either the dual imaging agents or the oleylamine-coated hafnia nanoparticles, the active ingredient for its CT performance is the hafnium element and quantified by hafnium mass. Therefore, a negligible effect from the FNP process is expected and the comparison conducted using HNCs should suffice. At 25 mM Hf, an increase of 29 HU is seen with the dual imaging agent compared to the HNCs in the Aquilion ONE GENESIS scanner. The signal difference is attributed to the extra SPIONs (57 mM) in the dual imaging agent at the above-mentioned concentration.

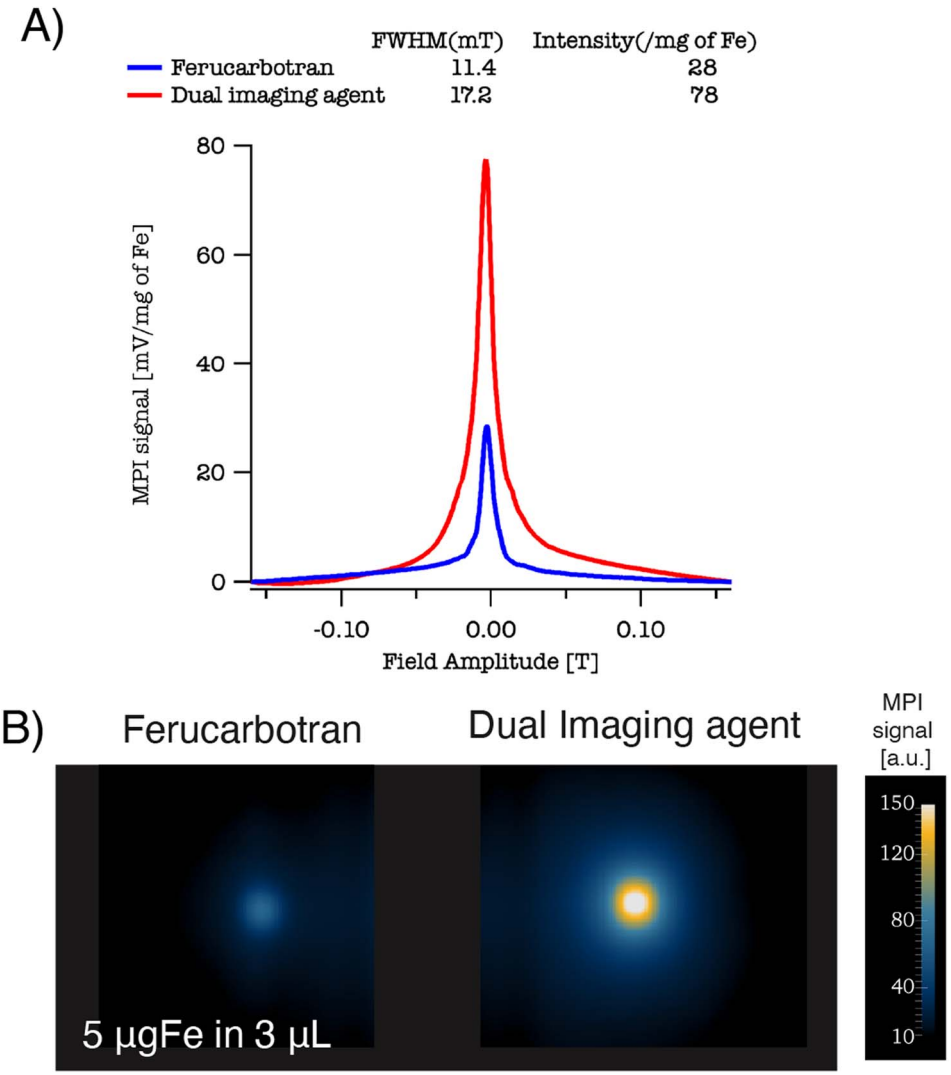

Fig. 4 (A) PSF for ferucarbotran and the dual imaging agents. (B) Side by side phantoms 2D isotropic images for ferucarbotran and dual imaging agents.

The CNR for both contrast agents in the Aquilion ONE GENESIS scanner using the SCT protocol is summarized in Table 2. The dual imaging agents have higher CNR at all concentrations compared to Omnipaque. As seen in Table 2, the CNRs for the lowest concentration (1 mM) of both contrast agents are below 3. According to Rose Criterion, the detection limit of an imaging system depends on CNR and a CNR must exceed 3–5 to be detectable.[33] This suggests that for both agents, 1 mM is below the detectable threshold. This likely contributes to the higher signal of Omnipaque compared to the dual imaging agents at 1 mM shown in Fig. 5.

Both contrast agents were evaluated in DECT using the Aquilion ONE GENESIS scanner. The monochromatic image (66 keV) is shown in Fig. 6A. The corresponding CT number and CNR for both contrast agents are plotted in Fig. 6B and C. According to the fitting, the signal intensity of the dual imaging agents was 1.6× Omnipaque in the DECT protocol, similar to that obtained using the SCT protocol. The CNR in DECT aligns with that observed in SCT, suggesting the dual imaging agents have higher CNR compared to Omnipaque. Even though the percentage difference in CNR in both systems (SCT and DECT) are comparable, the absolute value of CNR was lower in DECT compared to SCT. Fig. S5A† presents the iodine map for Omnipaque, the dual contrast agents, and a CT contrast agent produced by FNP using only PLA-*b*-PEG and the HNCs. Fig. S5B† illustrates the corresponding VNC, suggesting that DECT can differentiate signals from iodine and the hafnia-containing composite nanoparticles.

The benefit of dual-energy CT is that it can be used to produce a VMI that can differentiate between contrast agents and tissues. While many tissues with low atomic numbers appear with CT contrast that is virtually energy-independent, some contrast agents with high atomic numbers have energy-dependent CT contrast that can be used to encode composition information in the CT image.[34] This is true, for example, for iodine contrast agents for which the CT number

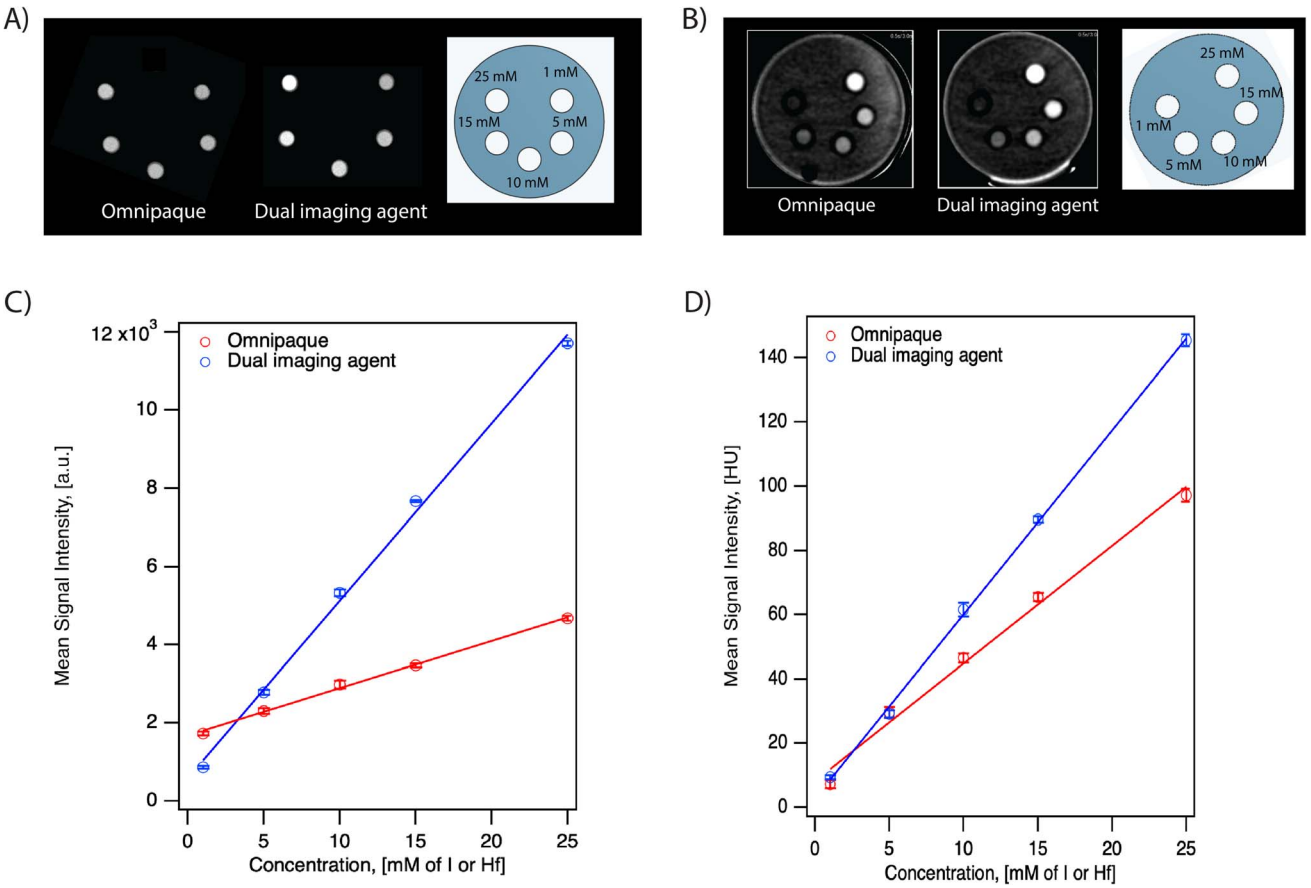

Fig. 5 Evaluation of CT performance of the dual imaging agents and Omnipaque at various concentrations in different scanners IVIS® Spectrum *In Vivo* Imaging System data is shown in (A) and (C) while Aquilion ONE GENESIS SCT data is shown in (B) and (D). Representative grayscale images for the dual imaging agents and Omnipaque at various concentrations were presented in (A) and (B), while quantitative data are presented in (C) and (D).

Table 2 Comparison of CNR of contrast agents and their percentage difference evaluated using different protocols in the clinical scanner

	SCT			DECT		
Concentration[a] [mmol]	Dual[b]	Omni[c]	Difference (%)	Dual[b]	Omni[c]	Difference (%)
25	141.5	63.9	121.3	28.4	18.2	56.2
15	84.5	41.5	103.7	16.4	10.4	58.1
10	55.9	28.0	99.7	11.5	7.1	62.6
5	22.9	16.0	43.3	5.4	2.6	109.7
1	2.6	0.13	186.1	0.41	0.23	76.6

[a] mmol of hafnium or iodine. [b] Dual represents dual imaging agents. [c] Omni represents Omnipaque.

decreases with increasing energy in the range typically used in CT scanners, enabling the generation of iodine maps that highlight the distribution of the contrast agent.[35] Fig. S6† shows the energy dependence of CT number for Omnipaque, the dual contrast agent, and the hafnia-only composite nanoparticles. Both Omnipaque and the dual imaging agent show CT numbers that decrease with increasing energy, albeit with different energy dependence for each contrast agent. In contrast, the nanoclusters containing hafnia nanoparticles alone have a CT number that is roughly independent of energy in the studied range. This suggests that composition maps similar to the iodine maps described above could be obtained for the dual imaging contrast agent. Furthermore, the reason for the higher signal of the dual imaging agents relative to Omnipaque in both the IVIS SpectrumCT and the Aquilion ONE GENESIS scanner becomes apparent from Fig. 6, where the CT number for the dual imaging agents is higher than that of Omnipaque.

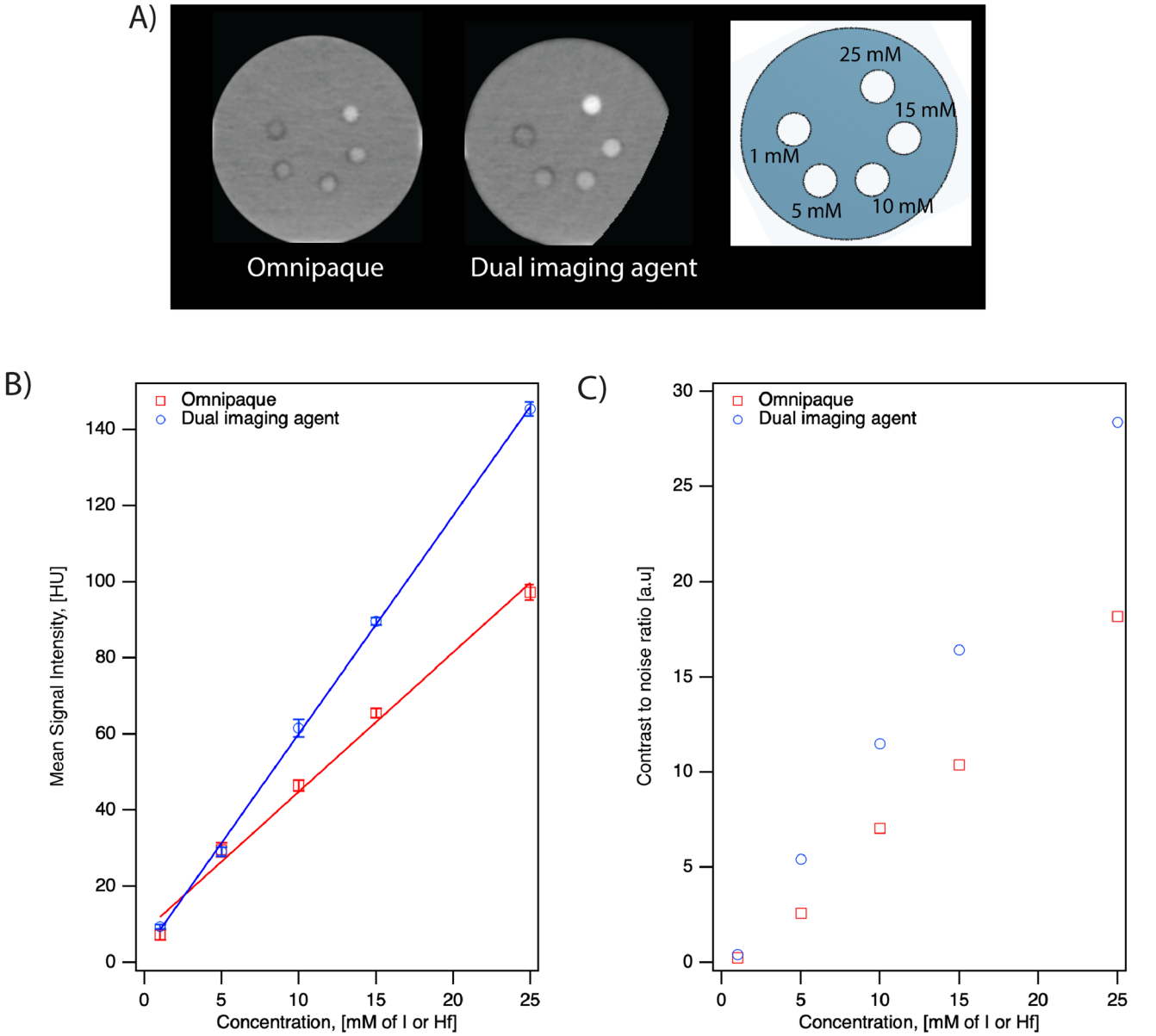

Fig. 6 Evaluation of CT performance in Aquilion ONE GENESIS scanner using a dual-energy CT. Representative grayscale CT images (A), CT performance at various concentrations (B), and CNR (C) of the dual imaging agents and Omnipaque.

4. Conclusions

We report the formulation of a first-of-its-kind dual imaging MPI/CT composite nanoparticle imaging agent. The agent consists of MPI-tailored SPIONs co-encapsulated with CT-contrast hafnia nanoparticles in composite nanoparticle clusters that contain the homopolymer PLA and an outer coating of the block copolymer PLA-*b*-PEG. This agent combines the quantitative sensitivity of MPI with the high-resolution and anatomical reference information that can be obtained from CT. The composite dual imaging agents were formulated using FNP, which is easy to scale up to quantities necessary for regulatory testing and clinical use. The physical and hydrodynamic properties of the formulated composite nanoparticles were evaluated. The MPI performance of the dual imaging agents was evaluated and compared to a commercial tracer ferucarbotran. Results suggest that the dual imaging agents has 3× sensitivity and slightly worse resolution. The worsening in resolution is attributed to the magnetic dipolar interaction between the magnetic nanoparticles in close proximity within the clusters. The hafnia-containing composite dual imaging agents also possess good CT contrast, relative to the commercially available clinical CT contrast agent Omnipaque, suggesting their suitability for CT. In addition, studies also suggest that the dual imaging agents are also good candidates for applications in dual-energy CT. Future studies will evaluate the applications of this novel composite MPI/CT dual imaging agent.

Author contributions

S. L. and C. R. R. conceived and designed the experiments. C. R. R. supervised the project and provided feedback. J. A. and I. B. helped in supervising the project and providing feedback. S. L. performed all nanomaterial synthesis, formulation, characterization, data acquisition and analysis. A. H. acquired clinical CT data and performed analysis. S. L. and C. R. R. wrote the manuscript. All authors discussed the result and commented on the manuscript.

Conflicts of interest

The authors have declared that no competing interest exists.

Acknowledgements

This was supported by the US National Science Foundation through grant DMR-1832733.

References

1 B. Gleich and R. Weizenecker, Tomographic imaging using the nonlinear response of magnetic particles, *Nature*, 2005, **435**, 1214–1217, DOI: **10.1038/nature03808**.
2 B. Zheng, *et al.*, Quantitative Magnetic Particle Imaging Monitors the Transplantation, Biodistribution, and Clearance of Stem Cells In Vivo, *Theranostics*, 2016, **6**, 291–301, DOI: **10.7150/thno.13728**.
3 B. Zheng, *et al.*, Magnetic Particle Imaging tracks the long-term fate of in vivo neural cell implants with high image contrast, *Sci. Rep.*, 2015, **5**, 14055, DOI: **10.1038/srep14055**.
4 E. Y. Yu, *et al.*, Magnetic Particle Imaging for Highly Sensitive, Quantitative, and Safe in Vivo Gut Bleed Detection in a Murine Model, *ACS Nano*, 2017, **11**, 12067–12076, DOI: **10.1021/acsnano.7b04844**.
5 E. G. Fuller, *et al.*, Theranostic nanocarriers combining high drug loading and magnetic particle imaging, *Int. J. Pharm.*, 2019, **572**, 118796, DOI: **10.1016/j.ijpharm.2019.118796**.
6 D. Hensley, *et al.*, Combining magnetic particle imaging and magnetic fluid hyperthermia in a theranostic platform, *Phys. Med. Biol.*, 2017, **62**, 3483–3500, DOI: **10.1088/1361-6560/aa5601**.
7 E. Y. Yu, *et al.*, Magnetic Particle Imaging: A Novel in Vivo Imaging Platform for Cancer Detection, *Nano Lett.*, 2017, **17**, 1648–1654, DOI: **10.1021/acs.nanolett.6b04865**.
8 P. Vogel, *et al.*, Magnetic Particle Imaging meets Computed Tomography: first simultaneous imaging, *Sci. Rep.*, 2019, **9**(1), 12627, DOI: **10.1038/s41598-019-48960-1**.
9 R. E. Alexander and R. B. Gunderman, EMI and the First CT Scanner, *J. Am. Coll. Radiol.*, 2010, **7**, 778–781, DOI: **10.1016/j.jacr.2010.06.003**.
10 L. C. Wu, *et al.*, A Review of Magnetic Particle Imaging and Perspectives on Neuroimaging, *Am. J. Neuroradiology*, 2019, **40**, 206–212, DOI: **10.3174/ajnr.A5896**.
11 P. Chandrasekharan, *et al.*, A perspective on a rapid and radiation-free tracer imaging modality, magnetic particle imaging, with promise for clinical translation, *Br. J. Radiol.*, 2018, **91**(1091), 20180326, DOI: **10.1259/bjr.20180326**.
12 J. Wang and D. Fleischmann, Improving Spatial Resolution at CT: Development, Benefits, and Pitfalls, *Radiology*, 2018, **289**, 261–262, DOI: **10.1148/radiol.2018181156**.
13 S. Liu, *et al.*, Long circulating tracer tailored for magnetic particle imaging, *Nanotheranostics*, 2021, **5**, 348–361, DOI: **10.7150/ntno.58548**.
14 T. Nowak, M. Hupfer, R. Brauweiler, F. Eisa and W. A. Kalender, Potential of high-Z contrast agents in clinical contrast-enhanced computed tomography, *Med. Phys.*, 2011, **38**, 6469–6482, DOI: **10.1118/1.3658738**.
15 T. L. McGinnity, *et al.*, Hafnia (HfO2) nanoparticles as an X-ray contrast agent and mid-infrared biosensor, *Nanoscale*, 2016, **8**, 13627–13637, DOI: **10.1039/c6nr03217f**.
16 J. F. Hainfeld, D. N. Slatkin, T. M. Focella and H. M. Smilowitz, Gold nanoparticles: a new X-ray contrast agent, *Br. J. Radiol.*, 2006, **79**, 248–253, DOI: **10.1259/bjr/13169882**.
17 *Gold Price*, **https://goldprice.org/**, 2022.
18 Current rare earth element price, **https://strategicmetalsinvest.com/current-strategic-metals-prices/#:~:text=ThecurrentpriceofHafniumis%241%2C741.10perkg**, 2022.
19 N. M. Pinkerton, *et al.*, Single-Step Assembly of Multimodal Imaging Nanocarriers: MRI and Long-Wavelength Fluorescence Imaging, *Adv. Healthcare Mater.*, 2015, **4**, 1376–1385, DOI: **10.1002/adhm.201400766**.
20 M. Unni, *et al.*, Thermal Decomposition Synthesis of Iron Oxide Nanoparticles with Diminished Magnetic Dead Layer by Controlled Addition of Oxygen, *ACS Nano*, 2017, **11**, 2284–2303, DOI: **10.1021/acsnano.7b00609**.
21 C. Liu, *et al.*, Facile Single-Precursor Synthesis and Surface Modification of Hafnium Oxide Nanoparticles for Nanocomposite -Ray Scintillators, *Adv. Funct. Mater.*, 2015, **25**, 4607–4616, DOI: **10.1002/adfm.201501439**.
22 J. Schindelin, *et al.*, Fiji: an open-source platform for biological-image analysis, *Nat. Methods*, 2012, **9**, 676–682, DOI: **10.1038/nmeth.2019**.
23 L. Maldonado-Camargo, M. Unni and C. Rinaldi, Magnetic Characterization of Iron Oxide Nanoparticles for Biomedical Applications, *Methods Mol. Biol.*, 2017, **1570**, 47–71, DOI: **10.1007/978-1-4939-6840-4_4**.
24 R. W. Chantrell, J. Popplewell and S. W. Charles, Measurements Of Particle-Size Distribution Parameters In Ferrofluids, *IEEE Transactions on Magnetics*, 1978, **14**, 975–977, DOI: **10.1109/tmag.1978.1059918**.
25 J. B. Birks, The Properties Of Ferromagnetic Compounds At Centimetre Wavelengths, *Proc. Phys. Soc., London, Sect. B*, 1950, **63**, 65–74, DOI: **10.1088/0370-1301/63/2/301**.
26 P. W. Goodwill, *et al.*, X-Space MPI: Magnetic Nanoparticles for Safe Medical Imaging, *Adv. Mater.*, 2012, **24**, 3870–3877, DOI: **10.1002/adma.201200221**.
27 H. Anahita, *et al.*, Contrast thresholds for detection of various iodine concentrations in subtraction CT and dual-

energy CT systems, *J. Appl. Clin. Med. Phys.*, 2022, **24**(1), e13834, DOI: **10.1002/acm2.13834**.

28 Y. Y. Li, *et al.*, Gram-scale synthesis of highly biocompatible and intravenous injectable hafnium oxide nanocrystal with enhanced radiotherapy efficacy for cancer theranostic, *Biomaterials*, 2020, **226**, 119538, DOI: **10.1016/j.biomaterials.2019.119538**.

29 M. Unni, *et al.*, Fast nanoparticle rotational and translational diffusion in synovial fluid and hyaluronic acid solutions, *Sci. Adv.*, 2021, **7**(27), DOI: **10.1126/sciadv.abf8467**.

30 S. Savliwala, S. T. Liu and C. M. Rinaldi-Ramos, Particle motion artifacts in equilibrium magnetization measurements of large iron oxide nanoparticles, *J. Magn. Magn. Mater.*, 2022, **547**, 168889, DOI: **10.1016/j.jmmm.2021.168889**.

31 R. Olayo-Valles and C. Rinaldi, Modulation of Interparticle Interactions and Specific Absorption Rate in Magnetomicelles through Changes in the Molecular Weight of the Hydrophobic Polymer Block, *Part. Part. Syst. Charact.*, 2013, **30**, 964–971, DOI: **10.1002/ppsc.201300157**.

32 L. R. Croft, P. W. Goodwill and S. M. Conolly, Relaxation in X-Space Magnetic Particle Imaging, *IEEE Trans. Med. Imaging*, 2012, **31**, 2335–2342, DOI: **10.1109/tmi.2012.2217979**.

33 S. R. Cherry, J. A. Sorenson and M. E. Phelps, *Physics in Nuclear Medicine*, Elsevier Science, 2012.

34 C. McCollough, *et al.*, Principles and applications of multienergy CT: Report of AAPM Task Group 291, *Med. Phys.*, 2020, **47**(7), e881–e912, DOI: **10.1002/mp.14157**.

35 D. Grob, *et al.*, Iodine Maps from Subtraction CT or Dual-Energy CT to Detect Pulmonary Emboli with CT Angiography: A Multiple-Observer Study, *Radiology*, 2019, **292**, 197–205, DOI: **10.1148/radiol.2019182666**.